

# Interactions between gravity waves and cirrus clouds: asymptotic modeling of wave induced ice nucleation

Stamen I. Dolaptchiev,<sup>a</sup> Peter Spichtinger,<sup>b</sup> Manuel Baumgartner,<sup>b</sup> and Ulrich Achatz<sup>a</sup>

<sup>a</sup> *Institut für Atmosphäre und Umwelt, Goethe-Universität Frankfurt, Frankfurt am Main, Germany*

<sup>b</sup> *Johannes Gutenberg-Universität Mainz, Mainz, Germany*

*Corresponding author:* Stamen Dolaptchiev, dolaptchiev@iau.uni-frankfurt.de

ABSTRACT: We present an asymptotic approach for the systematic investigation of the effect of gravity waves (GW) on ice clouds formed through homogeneous nucleation. In particular, we consider high- and mid-frequency GW in the tropopause region driving the formation of ice clouds, modeled with a double-moment bulk ice microphysics scheme. The asymptotic approach allows for identifying reduced equations for self-consistent description of the ice dynamics forced by GW including the effects of diffusional growth and nucleation of ice crystals. Further, corresponding analytical solutions for a monochromatic GW are derived under a single-parcel approximation. It is demonstrated that the asymptotic solutions capture to a high accuracy the dynamics of the reduced ice model during multiple nucleation events and provide a parameterization for the nucleated number of ice crystals. Extension of the present approach to allow for variable mean mass of the ice crystal distribution, as well as, implications for representation of GW variability in cirrus parameterizations are discussed.

## 1. Introduction

Clouds consisting exclusively of ice particles, so-called cirrus clouds, account for roughly one third of the total cloud cover, yet their net radiative effect is still one major source of uncertainty in the climate system. Since albedo effect and greenhouse effect are of the same order of magnitude for those clouds, microphysical details of ice crystals (as, e.g., shape or size, see Zhang et al. 1999; Krämer et al. 2020) may determine the net radiative effect. The microphysical properties, however, are strongly influenced by a complex interplay of nuclei composition, micro-scale cloud processes and multi-scale interactions with the surrounding atmosphere. All those components are poorly understood and, if at all, only crudely represented in coarse resolution models.

Cirrus clouds can be subdivided into liquid origin and in situ cirrus (e.g. Krämer et al. 2016). The former class describes clouds originating from cloud droplets, which freeze in upward motions, e.g., in mesoscale convective outflow or warm conveyor belts. In contrast, the ice crystals of in situ cirrus are formed without any pre-existing cloud droplets: either by homogeneous freezing of aqueous solution droplets (short: homogeneous nucleation, see, e.g., Koop et al. 2000; Baumgartner et al. 2022), or by heterogeneous nucleation (e.g. Pruppacher and Klett 2010; Hoose and Möhler 2012; Baumgartner et al. 2022) initiated by solid aerosol particles.

Observational studies indicate that cirrus properties and life cycle can be crucially affected by gravity wave (GW) dynamics (e.g. Kärcher and Ström 2003; Kim et al. 2016; Bramberger et al. 2022). GW are generated to a large fraction in the troposphere and often propagate over considerable horizontal and vertical distances before breaking. During their propagation those waves can generate substantial oscillations in the atmospheric fields and the GW drag, exerted in the breaking region, alters the mean atmospheric state. Because of the importance of small-scale GW dynamics some cirrus studies explicitly resolve the GW using LES models (e.g. Joos et al. 2009; Kienast-Sjögren et al. 2013), or detailed parcel models (e.g. Haag and Kärcher 2004; Jensen and Pfister 2004; Spichtinger and Krämer 2013). Other approaches, applicable in climate models, diagnose small-scale vertical velocities using a turbulent kinetic energy scheme (Lohmann and Kärcher 2002) and an orographic GW parameterization scheme (Dean et al. 2007; Joos et al. 2008). For an improved small-scale variability stochastic approaches were utilized (Wang and Penner 2010; Podglajen et al. 2016; Kärcher and Podglajen 2019), however the results strongly depend on the underlying statistical description. The studies listed above suggest that a complete

understanding of the GW influence on cirrus clouds is still missing. Such understanding is, however, required for the high-fidelity description of cirrus clouds in climate models.

Most of the current GW parameterizations in climate models rely on the single-column, steady-state approximation. Under this assumption GW propagate only in the vertical and instantly fast up to the breaking altitude, where they deposit energy and momentum. The limitations of steady-state parameterizations were demonstrated in the study by Bölöni et al. (2016), where a transient approach was proposed. The new transient parameterization was implemented by Bölöni et al. (2021) in the weather-forecast and climate model ICON, allowing to take into account intermittency effects in convectively generated GW (Kim et al. 2021). The transient parameterization has the potential for a more realistic representation of GW-cirrus interactions. This requires the systematic identification of the dominant interaction processes between GW and cirrus and their self-consistent description. Baumgartner and Spichtinger (2019) , hereafter BS19, utilized a matched-asymptotic approach for studying homogeneous nucleation due to constant updraft velocities. The resulting parameterization successfully reproduces the results of the classical scheme of Kärcher and Lohmann (2002). Encouraged by the results of BS19, we extend their asymptotic approach to allow for GW dynamics. We construct a self-consistent simplified model for GW-cirrus interactions and corresponding asymptotic solutions applicable for diagnosing ice crystal numbers in nucleation events forced by a passing GW.

This paper is organized as follows: The asymptotic representation of the GW and ice microphysics can be found in section 2. In section 3 we derive the reduced equations describing the GW and the cirrus dynamics. In addition, asymptotic solutions are constructed, modeling the nucleation, as well as, the pre- and post-nucleation dynamics. Numerical simulations of the reduced ice physics model and validation of the asymptotic solutions can be found in section 4. In section 5 the present approach is extended to take into account variations in the mean mass of the ice crystal distribution. Concluding discussions are summarized in section 6.

## 2. Asymptotic approach for studying GW-cirrus interactions

### a. Gravity wave dynamics: governing equations and scalings

Starting point are the equations governing a compressible flow on a  $f$ -plane (e.g. Durran 1989), without diabatic and frictional sources

$$\frac{d\mathbf{u}}{dt} + f\mathbf{e}_z \times \mathbf{u} = -c_p \theta \nabla_h \pi, \quad (1)$$

$$\frac{dw}{dt} = -c_p \theta \frac{\partial \pi}{\partial z} - g, \quad (2)$$

$$\frac{d\theta}{dt} = 0, \quad (3)$$

$$\frac{d\pi}{dt} + \frac{R\pi}{c_v} \nabla \cdot \mathbf{v} = 0. \quad (4)$$

Here, the total wind vector  $\mathbf{v}$  is separated into a horizontal,  $\mathbf{u}$ , and vertical,  $w$ , component,  $g$  denotes the gravitational acceleration,  $f$  the Coriolis parameter and  $\frac{d}{dt}$  the material derivative. In addition,  $c_p$  and  $c_v$  are the specific heat capacities of dry air at constant pressure and volume, respectively, and the ideal gas constant is given by  $R = c_p - c_v$ . Further,  $\theta$  denotes the potential temperature based on constant  $c_p$  (Baumgartner et al. 2020). The Exner pressure  $\pi$  is related to the pressure  $p$  by  $\pi = (p/p_{00})^{R/c_p}$ , where  $p_{00}$  is some reference pressure. The ideal gas law  $p/\rho = RT$  is assumed to be valid, where  $\rho$  is density and  $T$  temperature. We consider a hydrostatically balanced reference atmosphere at rest with pressure scale height,  $H_p$ , and potential temperature scale height,  $H_\theta$ , which depend on altitude and are defined by

$$H_p^{-1} = \left| \frac{1}{\bar{p}} \frac{d\bar{p}}{dz} \right| = \frac{g}{R\bar{T}}, \quad H_\theta^{-1} = \frac{1}{\bar{\theta}} \frac{d\bar{\theta}}{dz} = \frac{1}{\bar{T}} \left( \frac{d\bar{T}}{dz} + \frac{g}{c_p} \right). \quad (5)$$

In the last equations variables with an overbar refer to the reference atmospheric fields.

Within the framework of multiscale asymptotics, we have to specify a distinguished limit in order to define the regimes we are interested in, this is carried out in the following way:

First, we allow for weak and moderately strong stratification appropriate for the dynamics in the region of upper troposphere and lower stratosphere. Following Achatz et al. (2017), the different

stratifications can be expressed using the ratio

$$\frac{H_p}{H_\theta} = \varepsilon^\alpha, \quad \text{where } \varepsilon = O\left(10^{-1}\right) \quad \alpha = 0, 1. \quad (6)$$

In the equation above  $\alpha = 0$  corresponds to the strong and  $\alpha = 1$  to the weak stratification case.

Second, we specify the frequency regime of the GWs. In the analyses here the high- as well as mid-frequency GW are considered. Using the Brunt-Vaisala frequency  $N = \sqrt{\frac{g}{\theta} \frac{d\theta}{dz}}$  the reference GW time scale,  $T_w$ , is defined as

$$T_w = \frac{1}{\varepsilon^\beta N}, \quad \beta = 0, 1$$

where  $\beta = 0$  characterizes the high-frequency and  $\beta = 1$  the mid-frequency GW time scale. The corresponding GW period,  $P_w$ , is given by  $P_w = 2\pi T_w$ . For the vertical length scale of the GW,  $H_w$ , we assume (Achatz et al. 2010, 2017)

$$H_w = \varepsilon H_p. \quad (7)$$

The appropriate horizontal length scale,  $L_w$ , is estimated using the inertial GW dispersion relation (e.g. Achatz 2022)

$$\hat{\omega}^2 = \frac{f^2 m^2 + N^2 k_h^2}{k_h^2 + m^2}, \quad (8)$$

with  $\hat{\omega}$  the intrinsic GW frequency,  $m$  the vertical wavenumber and  $k_h$  the magnitude of the horizontal wave vector. By setting  $f/N = O\left(\varepsilon^{\frac{5-\alpha}{2}}\right)$ ,  $\hat{\omega} = 1/T_w$ ,  $m = 1/H_w$  and  $k_h = 1/L_w$  one obtains the estimate

$$L_w = \varepsilon^{-\beta} H_w. \quad (9)$$

Since the aspect ratio  $H_w/L_w$  defines the anisotropy of the GW, the high- and mid-frequency GW correspond to isotropic and moderately anisotropic waves, respectively. The reference quantity for the horizontal velocity scale,  $U$ , and for the vertical velocity scale,  $W$ , are estimated using the

advection velocities

$$U = \frac{L_w}{T_w}, \quad W = \frac{H_w}{T_w}. \quad (10)$$

As shown in Achatz et al. (2017) the above expressions are consistent with the polarization relations for GW if the mean flow entering the Doppler term is not larger than  $U$ . By introducing a reference temperature  $T_{00}$  such that

$$\bar{\theta} = O(T_{00}) \quad (11)$$

and using  $\bar{T} = O(T_{00})$ , one arrives at the expressions

$$H_p = O\left(\frac{RT_{00}}{g}\right), \quad U = O\left(\varepsilon^{\frac{2+\alpha}{2}} \sqrt{RT_{00}}\right), \quad W = O\left(\varepsilon^{\frac{2+\alpha+2\beta}{2}} \sqrt{RT_{00}}\right). \quad (12)$$

Using the above scaling for  $W$  we allow for strong and moderate vertical velocities: these are of the order of  $U$  in the case of high-frequency GW and of the order of  $\varepsilon U$  for the mid-frequency GW. The scalings presented in this section imply the following distinguished limit for the Mach, Froude and Rossby numbers

$$\text{Ma} = \frac{U}{\sqrt{RT_{00}}} \sim \varepsilon^{\frac{2+\alpha}{2}}, \quad \text{Fr} = \frac{U}{NH_p} \sim \varepsilon, \quad \text{Ro} = \frac{U}{fL_w} \sim \varepsilon^{\frac{2\beta+\alpha-5}{2}}. \quad (13)$$

The magnitude of the buoyancy GW fluctuations,  $B_w$ , is set to the one associated with GW close to breaking due to static instability (Achatz et al. 2010), namely

$$B_w = N^2 H_w = \varepsilon^{\alpha+1} g. \quad (14)$$

From the buoyancy definition  $b = g \frac{\theta - \bar{\theta}}{\bar{\theta}}$  one obtains for the magnitude of GW potential temperature fluctuations

$$\Theta_w = \varepsilon^{\alpha+1} T_{00}. \quad (15)$$

ref. quantity	value
$H_w$	$\varepsilon H_p = \varepsilon \frac{RT_{00}}{g}$
$T_w$	$\varepsilon^{-\beta} N^{-1}$
$L_w$	$\varepsilon^{1-\beta} H_p = \varepsilon^{1-\beta} \frac{RT_{00}}{g}$
$U$	$\varepsilon^{\frac{2+\alpha}{2}} \sqrt{RT_{00}}$
$W$	$\varepsilon^\beta U = \varepsilon^{\frac{2+\alpha+2\beta}{2}} \sqrt{RT_{00}}$
$\Theta_w$	$\varepsilon^{1+\alpha} T_{00}$
$\Pi_w$	$\varepsilon^{2+\alpha}$
$f$	$\varepsilon^{\frac{5-\alpha}{2}} N$

TABLE 1. Reference quantities for high-frequency,  $\beta = 0$ , and mid-frequency,  $\beta = 1$ , gravity wave scaling, where  $T_{00} = 210$  K,  $N = 10^{-2}$  s $^{-1}$  for the troposphere and  $N = 2 \times 10^{-2}$  s $^{-1}$  for the tropopause region.

Finally, as shown in Achatz et al. (2017) from the polarization GW relations, the GW pressure fluctuations scale as

$$\Pi_w \sim \frac{i}{m} \frac{\omega^2 - N^2}{N^2} \frac{B_w}{c_p \bar{\theta}} = O\left(\varepsilon^{2+\alpha}\right). \quad (16)$$

Nondimensionalizing the governing equations (1)-(4) with the reference quantities from Table 1 and replacing

$$(x, y, z, t, \nabla_h) \rightarrow (L_w x_w, L_w y_w, H_w z_w, T_w t_w, L_w^{-1} \nabla_h) \quad (17)$$

$$(\mathbf{u}, w, \theta, \pi, T, p) \rightarrow (U \mathbf{u}, W w, T_{00} \theta, \pi, T_{00} T, p_{00} p) \quad (18)$$

$$(f, g) \rightarrow (\varepsilon^{5/2} \frac{g}{\sqrt{RT_{00}}} f, g) \quad (19)$$

yields

$$\varepsilon^{2+\alpha} \frac{d\mathbf{u}}{dt_w} + \varepsilon^{\frac{9+\alpha}{2}-\beta} \mathbf{e}_z f \times \mathbf{u} = -\frac{c_p \theta}{R} \nabla_h \pi, \quad (20)$$

$$\varepsilon^{2+\alpha+2\beta} \frac{dw}{dt_w} = -\frac{c_p \theta}{R} \frac{\partial \pi}{\partial z_w} - \varepsilon, \quad (21)$$

$$\frac{d\theta}{dt_w} = 0, \quad (22)$$

$$\frac{d\pi}{dt_w} + \frac{R\pi}{c_v} \nabla \cdot \mathbf{v} = 0. \quad (23)$$

## b. Ice microphysics: governing equations and scalings

The cirrus clouds are described by a double-moment bulk microphysics scheme assuming an unimodal ice mass distribution function. The scheme is the same as the one from BS19, except that the sedimentational sinks are included here. A more detailed description of the ice model can be found in Spichtinger and Gierens (2009); Spreitzer et al. (2017), in this section we only briefly refer to some key properties. As in BS19 we assume spherical shape of ice crystals, which leads to a simpler description of the cloud processes.

The equations governing the ice crystal number concentration  $n$  (number of ice crystals per mass dry air, unit [ $\text{kg}^{-1}$ ]), ice mixing ratio  $q$  (mass of ice per mass dry air, unit [ $\text{kg}/\text{kg}$ ]) and vapor mixing ratio  $q_v$  (mass of water vapor per mass dry air, unit [ $\text{kg}/\text{kg}$ ]) read

$$\frac{dn}{dt} = Nuc_n + Sed_n \quad (24)$$

$$\frac{dq}{dt} = Dep + Nuc_q + Sed_q \quad (25)$$

$$\frac{dq_v}{dt} = -Dep - Nuc_q, \quad (26)$$

where  $Dep$  describes the ice crystal growth due to the deposition of water vapor,  $Nuc$  the generation of new ice crystals through homogeneous nucleation and  $Sed$  the sedimentation of ice crystals under the effect of gravity. The latter sedimentational processes are modeled as

$$Sed_n = \frac{1}{\rho} \frac{\partial}{\partial z} \rho v_n n, \quad (27)$$

$$Sed_q = \frac{1}{\rho} \frac{\partial}{\partial z} \rho v_q q, \quad (28)$$

where we assume spatially independent sedimentation velocities  $v_{n,q} = c_{n,q} m_{ref}^{2/3}$  with constants  $c_n = 5.8 \times 10^5$ ,  $c_q = 1.2 \times 10^6$  in units of  $\text{m s}^{-1} \text{kg}^{-2/3}$  and a reference mass  $m_{ref}$ ; this simplification is sufficient for estimating typical values of the sedimentation terms in the following asymptotic analysis.

In (25), (26) the deposition term  $Dep$ , also referred to as diffusional growth term, can be parameterized as

$$Dep = C_0 \bar{m}^{1/3} \frac{p_{si}}{p} (S - 1) T n \quad (29)$$

with  $C_0 = 4.3 \cdot 10^{-8} \text{ kg}^{2/3} \text{ s}^{-1} \text{ K}^{-1}$ ,  $p_{si}$  the saturation pressure over flat ice surface,  $\bar{m} = q/n$  the mean ice-particle mass and  $S$  the saturation ratio with respect to ice. The latter is defined as

$$S = \frac{p_v}{p_{si}},$$

where  $p_v$  is the water vapor pressure. Using the definition of  $q_v = m_v/m_d = \rho_v/\rho_d$  and the ideal gas law to express the dry air pressure,  $p_d = RT\rho_d$ , and the water vapor pressure,  $p_v = R_v T \rho_v$ , yields for the saturation ratio

$$S = \frac{q_v p_d}{\varepsilon_0 p_{si}} \approx \frac{q_v p}{\varepsilon_0 p_{si}}, \quad (30)$$

where  $\varepsilon_0 = R/R_v$  and the water vapor gas constant is given by  $R_v = 461 \text{ J kg}^{-1} \text{ K}^{-1}$ . The saturation pressure  $p_{si}$  is highly dependent on temperature and satisfies the approximate Clausius-Clapeyron equation

$$\frac{dp_{si}}{dT} = \frac{L_i}{R_v T^2} p_{si}$$

with  $L_i = 2.8 \times 10^6 \text{ J kg}^{-1}$ . In eq. (24) the homogeneous nucleation rate of ice crystals is modeled as

$$Nuc_n = J \exp(B(S - S_c)) \quad (31)$$

(following BS19 and Spichtinger et al. 2022), where  $S_c$  is some critical saturation ratio  $S_c(T) \approx 1.5$ ,  $J = 4.9 \cdot 10^4 \text{ kg}^{-1} \text{ s}^{-1}$  and  $B = 337$  (see BS19 for further details and the estimation of these values). The nucleation term in the equation for ice mixing ratio (25) is given by

$$Nuc_q = \hat{m}_0 Nuc_n, \quad (32)$$

quantity	value
$J$	$4.9 \times 10^4 \text{ kg}^{-1} \text{ s}^{-1}$
$B$	337
$S_c$	1.5
$C_0$	$4.3 \times 10^{-8} \text{ kg}^{2/3} \text{ s}^{-1} \text{ K}^{-1}$
$\varepsilon_0$	0.62
$c_n$	$5.8 \times 10^5 \text{ m s}^{-1} \text{ kg}^{-2/3}$
$c_q$	$12 \times 10^5 \text{ m s}^{-1} \text{ kg}^{-2/3}$
$\hat{m}_0$	$10^{-16} \text{ kg}$
$L_i$	$2.8 \times 10^6 \text{ J kg}^{-1}$
$R_v$	$461 \text{ J kg}^{-1} \text{ K}^{-1}$

TABLE 2. Parameters of the ice physics scheme

ref. quantity	value
$n_c$	$2 \times 10^6 \text{ kg}^{-1}$
$q_{v,c} = \frac{\epsilon_0 p_{si,c}}{p_{00}}$	$2 \times 10^{-5}$
$m_c$	$10^{-12} \text{ kg}$
$q_c = m_c n_c$	$2 \times 10^{-6}$
$T_d = \left( C_0 m_c^{1/3} \frac{p_{si,c}}{p_{00} q_{v,c}} T_{00} n_c \right)^{-1}$	400 s
$H_c$	600 m
$p_{00}$	300 hPa
$T_{00}$	210 K
$\rho_{00}$	$0.5 \text{ kg m}^{-3}$
$p_{si,c}(T_{00})$	1 Pa

TABLE 3. Reference quantities used for non-dimensionalization of the ice physics scheme

where the reference mass  $\hat{m}_0 = 10^{-16} \text{ kg} \ll \bar{m}$  is used, which represents a typical mass of newly nucleated ice crystals. A summary of the ice physics scheme parameters can be found in Tab. 2. Next, characteristic numbers for the ice physics variables are chosen. Those values should describe a typical cirrus cloud in the upper troposphere/ lower stratosphere region formed due to homogeneous nucleation. The characteristic values for the number concentration, vapor mixing ratio and ice mixing ratio are denoted by  $n_c$ ,  $q_{vc}$  and  $q_c$ , respectively. The estimate  $m_{ref} \sim \bar{m} \sim m_c$  is used, where  $m_c$  denotes some mean ice crystal mass satisfying  $q_c = n_c m_c$ . All reference values can be found in Tab. 3, they agree with the characteristic values used in BS19.

Next, we introduce a characteristic time scale on which the diffusional growth term acts, it is defined as

$$T_d = \left( C_0 m_c^{1/3} \frac{p_{si,c}}{p_{00} q_{v,c}} T_{00} n_c \right)^{-1} \sim 400 \text{ s}, \quad (33)$$

if the reference saturation pressure over ice  $p_{si,c} = 1 \text{ Pa}$  is used (see Tab. 3 for all other values). As can easily be shown, the estimate above for  $T_d$  allows for deviations of about 10 K from the reference temperature  $T_{00} = 210 \text{ K}$ . The characteristic vertical scale of the cirrus cloud is set to

$$H_c \sim H_w. \quad (34)$$

This corresponds to  $H_c = 600 \text{ m}$  for  $H_w$  from Tab. 1. Finally, the ice physics scheme is nondimensionalized using the reference quantities and all arising nondimensional numbers are expressed in terms of  $\varepsilon$  (distinguished limit), as summarized in Tab. 4. Applying the replacements

$$(z, t) \rightarrow (H_w z_w, T_d t_d) \quad (35)$$

$$(n, q, q_v, p_{si}, \rho) \rightarrow (n_c n, q_c q, q_{v,c} q_v, p_{si,c} p_{si}, \rho_{00} \rho) \quad (36)$$

one yields the following nondimensional equations

$$\frac{dn}{dt_d} = \frac{J^*}{\varepsilon} \exp\left(\frac{B^*}{\varepsilon^2}(S - S_c)\right) + \varepsilon^2 \frac{S_n^*}{\rho} \frac{\partial}{\partial z_w} \rho n \quad (37)$$

$$\frac{dq}{dt_d} = \frac{1}{\varepsilon} D^* \frac{p_{si}}{p} (S - 1) T n + \varepsilon^3 J^* \exp\left(\frac{B^*}{\varepsilon^2}(S - S_c)\right) + \varepsilon^2 \frac{S_q^*}{\rho} \frac{\partial}{\partial z_w} \rho q \quad (38)$$

$$\frac{dq_v}{dt_d} = -D^* \frac{p_{si}}{p} (S - 1) T n - \varepsilon^4 J^* \exp\left(\frac{B^*}{\varepsilon^2}(S - S_c)\right), \quad (39)$$

where an asterisk denotes an order one constant and  $\bar{m} \sim m_c$  was assumed in the deposition term.

One will also make use of the non-dimensional form of the Clausius-Clapeyron equation, which reads

$$\frac{dp_{si}}{dT} = \frac{L^*}{\varepsilon T^2} p_{si}. \quad (40)$$

quantity	value	distinguished limit
$B$	337	$\frac{B^*}{\varepsilon^2}$
$\frac{C_0 m_c^{1/3} T_{00} n_c T_w}{\varepsilon_0}$	1.456	$D^*$
$\frac{C_0 m_c^{1/3} T_{00} n_c T_w q_{v,c}}{\varepsilon_0 q_c^{2/3}}$	14.56	$\varepsilon^{-1} D^*$
$\frac{c_n m_c^{1/3} T_w}{H_c}$	$4.8 \times 10^{-3}$	$\varepsilon^3 S_n^*$
$\frac{c_q m_c^{2/3} T_w}{H_c}$	.01	$\varepsilon^2 S_q^*$
$\frac{J T_w}{n_c}$	12.5	$\frac{J^*}{\varepsilon}$
$\frac{\dot{m}_0 J T_w}{q_c}$	$1.2 \times 10^{-3}$	$\varepsilon^3 J^*$
$\frac{\dot{m}_0 J T_w}{q_{v,c}}$	$1.2 \times 10^{-4}$	$\varepsilon^4 J^*$
$\frac{L_i}{R \sqrt{T_{00}}}$	29	$\frac{L^*}{\varepsilon}$

TABLE 4. Distinguished limits for the non-dimensional numbers in the ice scheme. In the right-most column a star denotes an order one constant. For the nondimensionalization a time scale  $T_w$ , with  $T_w \sim T_d$ , was used.

Next, we derive from (39) an evolution equation for the saturation ratio  $S$ . Since,  $q_{v,c} = \varepsilon_0 p_{si,c} / p_{00}$  is used for the scaling of  $q_v$ , the definition of  $S$  expressed using nondimensional variables reads

$$S = \frac{q_v p}{p_{si}}. \quad (41)$$

Applying  $\frac{d}{dt_d}$  to (41) yields

$$\frac{dS}{dt_d} = \frac{p}{p_{si}} \frac{dq_v}{dt_d} + \frac{S}{p} \frac{dp}{dt_d} - \frac{S}{p_{si}} \frac{dp_{si}}{dt_d} \quad (42)$$

$$= \frac{p}{p_{si}} \frac{dq_v}{dt_d} + \frac{c_p S}{R \pi} \frac{d\pi}{dt_d} - \frac{S L^*}{\varepsilon T^2} \frac{dT}{dt_d} \quad (43)$$

$$= \frac{p}{p_{si}} \frac{dq_v}{dt_d} + \frac{c_p S}{R \pi} \frac{d\pi}{dt_d} - \frac{S L^*}{\varepsilon T^2} \left( \pi \underbrace{\frac{d\theta}{dt_d}}_{=0} + \theta \frac{d\pi}{dt_d} \right) \quad (44)$$

$$= \frac{p}{p_{si}} \frac{dq_v}{dt_d} - \frac{S}{\pi} \frac{d\pi}{dt_d} \left( \frac{L^*}{\varepsilon T} - \frac{c_p}{R} \right) \quad (45)$$

where (40) was used to obtain (43), (22) in (44) and the definition of potential temperature  $\theta = T/\pi$  for the last equation (45). Finally, the nondimensional system governing the ice dynamics reads

$$\frac{dn}{dt_d} = \frac{J^*}{\varepsilon} \exp\left(\frac{B^*}{\varepsilon^2}(S - S_c)\right) + \varepsilon^2 \frac{S_n^*}{\rho} \frac{\partial}{\partial z_w} \rho n \quad (46)$$

$$\frac{dq}{dt_d} = \frac{1}{\varepsilon} D^* \frac{p_{si}}{p} (S - 1) T n + \varepsilon^3 J^* \exp\left(\frac{B^*}{\varepsilon^2}(S - S_c)\right) + \varepsilon^2 \frac{S_q^*}{\rho} \frac{\partial}{\partial z_w} \rho q \quad (47)$$

$$\frac{dS}{dt_d} = -D^*(S - 1) T n - \frac{S}{\pi} \frac{d\pi}{dt_d} \left( \frac{L^*}{\varepsilon T} - \frac{c_p}{R} \right) - \varepsilon^4 \frac{p}{p_{si}} J^* \exp\left(\frac{B^*}{\varepsilon^2}(S - S_c)\right). \quad (48)$$

### c. Asymptotic expansion

The nondimensional coordinates  $\mathbf{x}_w, t_w$ , entering in equations (20)-(23), describe variations on the GW spatial and temporal scales. In order to take into account variations of the reference atmosphere on the large, i.e. synoptic, vertical scale,  $H_s$ , with  $H_s \sim H_p = H_w/\varepsilon$ , we introduce a compressed coordinate defined as

$$z_s = \varepsilon z_w. \quad (49)$$

We consider a wave field (denoted by a prime) superimposed on a hydrostatically balanced reference atmosphere (denoted by a bar)

$$\theta = \bar{\theta}(z_s) + \varepsilon^{1+\alpha} \theta'(\mathbf{x}_w, t_w) \quad (50)$$

$$\pi = \bar{\pi}(z_s) + \varepsilon^{2+\alpha} \pi'(\mathbf{x}_w, t_w) \quad (51)$$

$$\mathbf{v} = \mathbf{v}'(\mathbf{x}_w, t_w) \quad (52)$$

where we have used the scaling from (15), (16). Next, in accordance with (6) the potential temperature of the reference atmosphere is expanded as

$$\bar{\theta}(z_s) = \begin{cases} \bar{\theta}^{(0)}(z_s) + O(\varepsilon) & \text{if } \alpha = 0 \\ 1 + \varepsilon \bar{\theta}^{(1)}(z_s) + O(\varepsilon^2) & \text{if } \alpha = 1 \end{cases}, \quad (53)$$

whereas the corresponding Exner pressure expansion reads

$$\bar{\pi}(z_s) = \sum_{j=0}^{1+\alpha} \varepsilon^j \bar{\pi}^{(j)}(z_s) + O(\varepsilon^{\alpha+2}). \quad (54)$$

For the wave part we make a wave ansatz, e.g. for the potential temperature field it reads

$$\theta'(\mathbf{x}_w, t_w) = \operatorname{Re} \left\{ \tilde{\theta}^{(1+\alpha)} \exp[i(\mathbf{k} \cdot \mathbf{x}_w - \omega t_w)] \right\} + O(\varepsilon), \quad (55)$$

with the wave amplitude  $\tilde{\theta}^{(1+\alpha)}$ , the wave vector  $\mathbf{k} = (k, l, m)^T$  and the frequency  $\omega$ . Further, consistent with the definitions of the potential temperature and Exner pressure one obtains

$$(T, \rho) = (\bar{T}, \bar{\rho})(z_s) + \varepsilon^{1+\alpha} (T', \rho')(\mathbf{x}_w, t_w, z_s) \quad (56)$$

$$p = \bar{p}(z_s) + \varepsilon^{2+\alpha} p'(\mathbf{x}_w, t_w, z_s). \quad (57)$$

The following asymptotic expansion for the ice fields  $\chi = (n, q, S)$  is used

$$\chi = \chi^{(0)} + O(\varepsilon), \quad (58)$$

in addition  $S_c = O(1)$  is assumed. Integrating (40) with the boundary condition  $p_{si}(1) = 1$  (or in dimensional form  $p_{si}(T_{00}) = p_{si,c}$ ), one obtains for the saturation pressure over ice

$$p_{si}(T) = \exp \left\{ \frac{L^*}{\varepsilon} \left( 1 - \frac{1}{\bar{T} + \varepsilon^{1+\alpha} T'} \right) \right\}. \quad (59)$$

In the next section we will consider the ice physics at the reference height  $z_{00}$ , at this level we have

$$\bar{p}^{(0)} = \bar{T}^{(0)} = \bar{\rho}^{(0)} = \bar{\theta}^{(0)} = \bar{\pi}^{(0)} = 1 \quad (60)$$

and from (59):  $p_{si}(z_{00}) = O(1)$ .

*d. Coupling of the GW and diffusion time scale*

We consider the following distinguished limit for the GW time scale,  $T_w$ , and for the diffusion time scale,  $T_d$ ,

$$\frac{T_d}{T_w} = O(1) . \quad (61)$$

Since  $T_d = 400$  s, the scaling above is valid for mid-frequency GW in the troposphere and stratosphere, as well, for high-frequency GW in the troposphere. In the case of mid-frequency GW one has  $T_w \sim 10^3$  s in the troposphere and  $T_w \sim 500$  s in the tropopause region, if the Doppler term in the GW dispersion relation is neglected. In the case of high-frequency GW in the troposphere one has  $T_w \sim 100$  s. Note, that the corresponding GW period,  $P_w$ , reads  $P_w = 2\pi T_w$ . The case  $T_d/T_w = O(\varepsilon)$ , relevant for low-frequency GW, leads to a weak amplitude GW forcing and will be presented in an upcoming study. The condition (61) together with (51) yields the transformation

$$\frac{d\pi}{dt_d} = \left( \varepsilon^{2+\alpha} \frac{d\pi'}{dt_w} + \varepsilon w \frac{d\bar{\pi}}{dz_s} \right) \quad (62)$$

Eq. (61) implies that the coordinates  $t_w$  and  $t_d$  resolve variations on the same time scale, hence we may identify these two and replace  $t_d$  in the following by  $t_w$ .

*e. Single parcel model approximation and single monochromatic GW*

In the following we adopt a Lagrangian framework and consider the ice physics of a single air parcel influenced by GW dynamics. Further, we assume that the leading order vertical velocity in (62) is solely due to a single GW and can be written as

$$w^{(0)}(t_w) = |\tilde{w}^{(0)}| \cos(\omega t_w + \phi) , \quad (63)$$

with the real amplitude  $|\tilde{w}^{(0)}|$  and the phase  $\phi$ .

### 3. Reduced model of GW-cirrus interactions

#### a. GW dynamics

From the leading order continuity equation we obtain

$$\nabla \cdot \mathbf{v}^{(0)} = 0. \quad (64)$$

Using the wave ansatz for  $\mathbf{v}^{(0)}$ , this gives the solenoidality condition

$$\mathbf{k} \cdot \tilde{\mathbf{v}}^{(0)} = 0, \quad (65)$$

implying that the wave vector  $\mathbf{k}$  and  $\tilde{\mathbf{v}}^{(0)}$  are orthogonal. The latter property will be used to eliminate various nonlinear advection terms in the equations.

From the leading order vertical momentum equation we obtain hydrostatic balance between  $\bar{\pi}^{(0)}$  and  $\bar{\theta}^{(0)}$

$$\frac{d\bar{\pi}^{(0)}}{dz_s} = -\frac{R}{c_p \bar{\theta}^{(0)}}. \quad (66)$$

Similarly, the next order vertical momentum balance reads

$$\frac{d\bar{\pi}^{(1)}}{dz_s} = \frac{R\bar{\theta}^{(1)}}{c_p \bar{\theta}^{(0)2}}, \quad (67)$$

where we have used (66). Note, that in the case  $\alpha = \beta = 0$  there is no advection term appearing in the latter equation due to (65).

The projection of the leading order equations onto the GW field reads

$$\frac{\partial \mathbf{u}^{(0)}}{\partial t_w} = -\frac{c_p \bar{\theta}^{(0)}}{R} \nabla_h \pi^{(2+\alpha)} \quad (68)$$

$$(1-\beta) \frac{\partial w^{(0)}}{\partial t_w} = -\frac{c_p \bar{\theta}^{(0)}}{R} \frac{\partial \pi^{(2+\alpha)}}{\partial z_w} + \frac{\theta^{(1+\alpha)}}{\bar{\theta}^{(0)}} \quad (69)$$

$$\nabla_w \cdot \mathbf{v}^{(0)} = 0, \quad (70)$$

$$\frac{\partial \theta^{(1+\alpha)}}{\partial t_w} + w^{(0)} \frac{d\bar{\theta}^{(\alpha)}}{dz_s} = 0, \quad (71)$$

where again (65) was utilized. Inserting in eqs. (68)-(71) a wave ansatz for the solution, one obtains the following system of linear equations for the wave amplitudes

$$\mathbf{M}\mathbf{z} = 0 \quad (72)$$

where

$$\mathbf{M} = \begin{pmatrix} -i\omega & 0 & 0 & 0 & ik \\ 0 & -i\omega & 0 & 0 & il \\ 0 & 0 & -i(1-\beta)\omega & -\bar{N} & im \\ 0 & 0 & \bar{N} & -i\omega & 0 \\ ik & il & im & 0 & 0 \end{pmatrix} \quad (73)$$

with  $\mathbf{z} = (\tilde{u}^{(0)}, \tilde{v}^{(0)}, \tilde{w}^{(0)}, \tilde{b}^{(1+\alpha)}/\bar{N}, \frac{c_p}{R} \bar{\theta}^{(0)} \tilde{\pi}^{(2+\alpha)})$ ,  $\bar{N}^2 = \frac{1}{\bar{\theta}^{(0)}} \frac{d\bar{\theta}^{(\alpha)}}{dz}$  and  $\tilde{b}^{(1+\alpha)} = \tilde{\theta}^{(1+\alpha)}/\bar{\theta}^{(0)}$ . Looking for non-trivial solutions of (72), one derives the dispersion relation

$$\omega^2 = \bar{N}^2 \frac{k^2 + l^2}{m^2 + (1-\beta)(k^2 + l^2)}, \quad (74)$$

and the polarization relations for the GW amplitudes

$$(\tilde{u}^{(0)}, \tilde{v}^{(0)}, \tilde{w}^{(0)}, \tilde{\pi}^{(2+\alpha)}) = -\frac{im\omega}{k_h^2 N^2} \tilde{b}^{(1+\alpha)} \left( k, l, -\frac{k_h^2}{m}, \frac{\omega R}{c_p \bar{\theta}^{(0)}} \right). \quad (75)$$

### b. The different regimes in the ice dynamics

The gravity wave dynamics changes the vertical velocity, pressure and temperature fields in (48) and hence leads to variations of  $S$  and consequently of  $n$ . Time series illustrating the qualitative behavior of  $S$  and  $n$  under GW forcing are shown in Fig. 1, see the discussion in section 4 for details. A typical situation observed is that  $S$  fluctuates until it reaches (or approaches sufficiently) the critical value  $S_c$  at time  $t_0$  (denoted by the vertical line in the plot of  $S$  at around  $t = 6$ ). At  $t_0$  the nucleation term in (46) leads to an explosive production of ice crystals. The increased number concentration  $n$  implies a reduction of  $S$  below  $S_c$  through the diffusional growth term in (48). After this reduction  $S$  continues to fluctuate due to the GW forcing and might again reach  $S_c$ , e.g.,

see the right panel of Fig. 2. Thus, in some cases we have to consider ice nucleation in presence of pre-existing ice crystals, which might be suppressed under certain conditions.

Following the matched asymptotic approach of BS19, three different regimes are considered here. First, the pre-nucleation regime with  $S < S_c$ , where the dynamics takes place on the GW time scale. This is followed by a nucleation regime, centered around time  $t_0$  with  $S(t_0) = S_c$  and dynamics on the much faster nucleation time scale. After the nucleation event the post-nucleation regime is entered with  $S < S_c$ , characterized again by dynamics on the GW time scale.

We observe that due to the assumption  $\bar{m} = m_c$  the evolution of  $n$  and  $S$  is decoupled from the one of  $q$ . Because of this we first consider equations (46) and (48). Once  $n$  and  $S$  are known,  $q$  can be found from (47). The case where all three equations (46), (47) and (48) are coupled is discussed in Sec. 5.

### c. Pre- and post-nucleation regime

Because the dynamics in the pre- and post-nucleation regime takes place at the same characteristic time scale, we treat them simultaneously here. In both regimes  $S$  is below the critical value,  $S < S_c$ , and  $S - S_c = O(1)$  even in the limit  $\varepsilon \rightarrow 0$ . This implies that the nucleation term in (46) is transcendentally small

$$\frac{J^*}{\varepsilon} \exp\left(\frac{B^*}{\varepsilon^2}(S - S_c)\right) \rightarrow 0 \text{ for } \varepsilon \rightarrow 0. \quad (76)$$

Next, we substitute in (46), (48) the expansion (58) for  $n$ ,  $S$  and collect the leading order terms. Evaluating the resulting equations at  $z_{00}$  gives

$$\frac{dn^{(0)}}{dt_w} = 0, \quad (77)$$

$$\frac{dS^{(0)}}{dt_w} = -D^*(S^{(0)} - 1)n^{(0)} + A^*S^{(0)} \cos(\omega t_w + \phi), \quad (78)$$

where (60), (62), (63), (66) are used and the amplitude of the GW forcing term is defined as

$$A^* = \frac{RL^*|\tilde{w}^{(0)}|}{c_p}. \quad (79)$$

From (77) one obtains that the number concentration does not change with time

$$n^{(0)} = \begin{cases} N_{pre} & \text{in the pre-nucleation regime} \\ N_{post} & \text{in the post-nucleation regime} \end{cases} . \quad (80)$$

Whereas the constant  $N_{pre}$  is typically given by the initial condition, the number concentration after the nucleation,  $N_{post}$ , is at this stage unknown. By integrating (78) from the initial time  $t_*$  up to  $t_w$ , one obtains an integral representation for  $S^{(0)}$

$$S^{(0)}(t_w) = S_* S_h(t_w, t_*) + \int_{t_*}^{t_w} dt' D^* n^{(0)} S_h(t_w, t') , \quad (81)$$

where the propagator  $S_h(t_w, t_*)$  is defined as

$$S_h(t_w, t_*) = \exp \left\{ \left[ -D^* n^{(0)} t + \frac{A^*}{\omega} \sin(\omega t + \phi) \right]_{t_*}^{t_w} \right\} \quad (82)$$

and the constant  $S_* = S(t_*)$  is given by the initial condition for the saturation ratio.

#### *d. Nucleation regime*

The nucleation regime is around the (unknown) time  $t_0$ , when the pre-nucleation  $S^{(0)}$  reaches the critical value  $S_c$

$$S^{(0)}(t_0) = S_c , \quad (83)$$

and it is characterized by the condition  $S - S_c = O(\varepsilon^2) > 0$ . The  $\varepsilon^{-2}$  scaling in the exponent of the nucleation term in (46) indicates that the dynamics during nucleation evolves on a fast time scale. This motivates to introduce a rescaled time coordinate

$$\tau = \frac{t_w - t_0}{\varepsilon^2} . \quad (84)$$

Equations (46) and (48) are expressed in terms of  $\tau$  giving

$$\frac{dn}{d\tau} = \varepsilon J^* \exp\left(\frac{B^*}{\varepsilon^2}(S - S_c)\right) + \varepsilon^4 \frac{S_n^*}{\rho} \frac{\partial}{\partial z_w} \rho n \quad (85)$$

$$\frac{dS}{d\tau} = \varepsilon^2 \left[ -D^*(S-1)Tn - \frac{S}{\pi} \left( \varepsilon^{2+\alpha} \frac{d\pi'}{dt_w} + \varepsilon w \frac{d\bar{\pi}}{dz_s} \right) \left( \frac{L^*}{\varepsilon T} - \frac{c_p}{R} \right) - \varepsilon^4 \frac{p}{p_{si}} J^* \exp\left(\frac{B^*}{\varepsilon^2}(S - S_c)\right) \right]. \quad (86)$$

The last two equations can be written in compact form as

$$\frac{dn}{d\tau} = \varepsilon J^* \exp\left(\frac{B^*}{\varepsilon^2}(S - S_c)\right) + O(\varepsilon^4) \quad (87)$$

$$\frac{dS}{d\tau} = \varepsilon^2 \left[ -D^*(S-1)Tn - \frac{L^* S w}{\bar{\pi}} \frac{d\bar{\pi}}{dz_s} \right] + O(\varepsilon^3), \quad (88)$$

where the nucleation term in (86) was eliminated using (85). From the leading order of (88) one obtains that the saturation ratio  $S^{(0)}$  does not change during nucleation

$$\frac{dS^{(0)}}{d\tau} = 0 \rightarrow S^{(0)}(\tau) = S_c, \quad (89)$$

consistent with (83). Next, the equation for  $n$  is considered: first (87) is differentiated with respect to  $\tau$  and after this the exponential function is replaced using (87) giving

$$\frac{d^2n}{d\tau^2} = \frac{B^*}{\varepsilon^2} \frac{dS}{d\tau} \frac{dn}{d\tau} + O(\varepsilon^2). \quad (90)$$

Inserting (88) yields

$$\frac{d^2n}{d\tau^2} = B^* \frac{dn}{d\tau} \left[ -D^*(S-1)Tn - \frac{L^* S w}{\bar{\pi}} \frac{d\bar{\pi}}{dz_s} \right] + O(\varepsilon). \quad (91)$$

The evaluation of the leading order equation takes the form

$$\frac{d^2n^{(0)}}{d\tau^2} = B^* \frac{dn^{(0)}}{d\tau} \left[ -D^*(S^{(0)}-1)\bar{T}^{(0)}n^{(0)} - \frac{L^* S^{(0)} w^{(0)}}{\bar{\pi}^{(0)}} \frac{d\bar{\pi}^{(0)}}{dz_s} \right]. \quad (92)$$

After substituting (60), (63), (66) and (79) in the last equation one yields

$$\frac{d^2n^{(0)}}{d\tau^2} = B^* \frac{dn^{(0)}}{d\tau} \left[ -D^*(S^{(0)}-1)n^{(0)} + A^* S^{(0)} \cos(\omega t_0 + \phi) \right], \quad (93)$$

where the expansion:  $\cos(\omega t + \phi) = \cos(\omega t_0 + \phi) + O(\varepsilon^2)$  was used. Taking into account that  $S^{(0)} = S_c$ , equation (93) can be written as

$$\frac{d}{d\tau} \left( \frac{dn^{(0)}}{d\tau} + \delta(n^{(0)})^2 - \gamma n^{(0)} \right) = 0 \quad (94)$$

where the following constants are introduced

$$\delta = \frac{1}{2} B^* D^* (S_c - 1) \quad (95)$$

$$\gamma = A^* B^* S_c \cos(\omega t_0 + \phi). \quad (96)$$

Integrating (94) yields

$$\frac{dn^{(0)}}{d\tau} + \delta(n^{(0)})^2 - \gamma n^{(0)} = \mu, \quad (97)$$

with the constant of integration  $\mu$ . Integrating (97) from 0 up to some time  $\tau$ , one obtains for the number concentration in the nucleation regime

$$n^{(0)}(\tau) = \frac{n_s + n_e C e^{\sigma\tau}}{1 + C e^{\sigma\tau}}, \quad (98)$$

with the constants

$$\sigma = \sqrt{\gamma^2 + 4\delta\mu} \quad (99)$$

$$n_s = \frac{\gamma - \sigma}{2\delta} \quad (100)$$

$$n_e = \frac{\sigma + \gamma}{2\delta} \quad (101)$$

$$C = \frac{n_0 - n_s}{n_e - n_0} \quad (102)$$

and another constant of integration  $n_0 = n^{(0)}(0)$ .

#### e. Matching

Next, we find the constants of integration, entering the solution in the nucleation and the post-nucleation regime by matching the different solutions in the pre-nucleation, nucleation and post-

nucleation regime. First, we consider the limits  $\tau \rightarrow \pm\infty$  of the nucleation solution (98)

$$n_{nuc}^{(0)}(-\infty) = n_s \quad (103)$$

$$n_{nuc}^{(0)}(\infty) = n_e \quad (104)$$

$$\frac{dn_{nuc}^{(0)}}{d\tau}(\pm\infty) = 0. \quad (105)$$

The nucleation solution for the number concentration,  $n_{nuc}(\tau)$ , should match for  $\tau \rightarrow -\infty$  the one from the pre-nucleation regime,  $n_{pre}^{(0)}(t)$ , for  $t \rightarrow t_0$ . Equating (103) and (80) give

$$n_s = N_{pre}. \quad (106)$$

By considering (97) for  $\tau \rightarrow -\infty$  one obtains with the help of (103), (105) and (106)

$$\mu = \delta N_{pre}^2 - \gamma N_{pre}. \quad (107)$$

Matching the saturation ratio in the nucleation regime,  $S_{nuc}^{(0)}$  from (89), to the one in the pre-nucleation regime,  $S_{pre}^{(0)}$  from (81), gives the condition

$$S_* S_h(t_0, t_*) + \int_{t_*}^{t_0} dt' D^* N_{pre} S_h(t_0, t') = S_c. \quad (108)$$

The last equation is an implicit equation for the time of the nucleation event  $t_0$ , where  $S_h(t_0, t_*) = \exp \left\{ \left[ -D^* N_{pre} t + \frac{A^*}{\omega} \sin(\omega t + \phi) \right]_{t_*}^{t_0} \right\}$  and  $S_*$  is given by the initial condition.

Next, the nucleation solution for the number concentration,  $n_{nuc}(\tau)$ , should match for  $\tau \rightarrow \infty$  the one from the post-nucleation regime,  $n_{post}^{(0)}(t)$ , for  $t \rightarrow t_0$ . Equating (104) and (80) gives

$$n_e = N_{post}. \quad (109)$$

From (101), with  $\sigma$  and  $\mu$  given by (99) and (107), respectively, the post-nucleation value for the number concentration can be found

$$N_{post} = \begin{cases} \frac{2A^*S_c \cos(\omega t_0 + \phi)}{D^*(S_c - 1)} - N_{pre} & \text{if } N_{pre} < \frac{A^*S_c \cos(\omega t_0 + \phi)}{D^*(S_c - 1)} \\ N_{pre} & \text{else} \end{cases}. \quad (110)$$

The two cases in the last solution result from the condition that the expression under the root in (99) is positive. Eq (110) implies that there are newly nucleated ice crystals only for  $N_{pre} < N_{pre}^c = \frac{A^*S_c \cos(\omega t_0 + \phi)}{D^*(S_c - 1)}$ . In the case of nucleation the larger  $N_{pre}$  the smaller  $N_{post}$  is, however the average  $(N_{pre} + N_{post})/2$  does not depend on the initial  $n$  and is always the same (for fixed  $t_0$  and  $A^*$ ). Interestingly, the threshold  $N_{pre}^c$  has important implication for the pre-nucleation dynamics of the saturation ratio. For  $N_{pre} > N_{pre}^c$  most likely the necessary condition  $S = S_c$  for the existence of nucleation will not be met. Since  $S$  is increasing just before nucleation, one has  $\dot{S} > 0$  at time  $t_0$  when  $S = S_c$ . From (78) this leads again to the condition  $N_{pre} < N_{pre}^c$  for a nucleation, if  $\cos(\omega t_0 + \phi) > 0$  is assumed. Eq. (110) defines further for  $\cos(\omega t_0 + \phi) = 1$  two interesting limits

$$N_{post}^{max} = \frac{2A^*S_c}{D^*(S_c - 1)} - N_{pre} \quad (111)$$

$$N_{pre}^{max} = \frac{A^*S_c}{D^*(S_c - 1)}. \quad (112)$$

$N_{post}^{max}$  is the maximum possible post-nucleation number concentration due to a GW with a given amplitude.  $N_{pre}^{max}$  is the maximum possible pre-nucleation number concentration which might allow for a nucleation (see also the discussion on pre-existing ice in Gierens 2003). In section 4b it will be shown that the latter number is a good approximation of the minimum post-nucleation number concentration observed in simulations.

Despite the fact that  $N_{post}$  is determined from (110), the integration constant  $n_0$  entering (98) through (102) is still unknown. It will, however, not effect the value of  $N_{post}$ . Moreover, since in the present asymptotic analysis  $t_0$  can be found up to some higher order corrections,  $n_0$  is undetermined. To see this we introduce another constant  $\tau_0$  defined as  $C = e^{-\sigma\tau_0}$ , we can write

(98) as

$$n^{(0)}(\tau) = \frac{n_s + n_e e^{\frac{\sigma}{\varepsilon^2}(t-t_0-\varepsilon^2\tau_0)}}{1 + e^{\frac{\sigma}{\varepsilon^2}(t-t_0-\varepsilon^2\tau_0)}} \quad (113)$$

Note, that from (108)  $t_0$  is determined up to  $O(\varepsilon)$  corrections, which will result in modifications of the constant  $n_0$ . One way of setting the value for  $n_0$  is by requiring that at  $\tau = 0$  the saturation ratio  $S$  should reach a maximum. At the end of the pre-nucleation we have  $\dot{S} > 0$ , on the other hand at the beginning of the post-nucleation  $\dot{S} < 0$ , thus  $S$  should have a maximum within the nucleation regime. We define  $n_0$  by requiring that in (88)  $\dot{S} = 0$  at time  $\tau = 0$  up to  $O(\varepsilon^3)$  corrections. After using (60), (63), (66) (79) and (89) this implies

$$n_0 = \frac{\gamma}{2\delta} = \frac{A^* S_c \cos(\omega t_0 + \phi)}{D^*(S_c - 1)} \implies C = 1. \quad (114)$$

The requirement of having a maximum in the saturation ratio upon the nucleation is physically meaningful and may be interpreted as the defining feature of a nucleation event.

#### *f. Composite solution and dimensional form of the asymptotic model*

It remains to construct the composite solution valid in all three regimes. For the number concentration the nucleation regime represents an interior layer (e.g. Holmes 2013), enclosed by the outer layers of the pre-nucleation and post-nucleation regime. In this case the composite solution reads

$$n(t_w) = n_{pre}^{(0)}(t_w) + n_{nuc}^{(0)}(\tau) + n_{post}^{(0)}(t_w) - n_{nuc}^{(0)}(-\infty) - n_{nuc}^{(0)}(\infty) + O(\varepsilon). \quad (115)$$

Substituting (80), (98), (103) and (104) in (115) gives for the number concentration

$$n(t_w) = \frac{n_s + n_e e^{\frac{\sigma}{\varepsilon^2}(t_w-t_0)}}{1 + e^{\frac{\sigma}{\varepsilon^2}(t_w-t_0)}} + O(\varepsilon). \quad (116)$$

Since the time derivative of the saturation ratio has a jump from the pre-nucleation to the post-nucleation value, the nucleation regime represents a corner layer for  $S$  (Holmes 2013). For such a layer two cases depending on the sign of  $t - t_0$  has to be considered when constructing the composite

solution

$$S(t_w) = \begin{cases} S_{pre}^{(0)}(t_w) + S_{nuc}^{(0)}(\tau) - S_{nuc}^{(0)}(-\infty) & \text{for } t_w \leq t_0 \\ S_{post}^{(0)}(t_w) + S_{nuc}^{(0)}(\tau) - S_{nuc}^{(0)}(\infty) & \text{for } t_w > t_0 \end{cases} + O(\varepsilon). \quad (117)$$

Substituting (81), (89) in (117), the solution for  $S$  takes the form

$$S(t_w) = \begin{cases} S_* S_h(t_w, t_*) + \int_{t_*}^{t_w} dt' D^* n_s S_h(t_w, t') & \text{for } t_w \leq t_0 \\ S_c S_h(t_w, t_0) + \int_{t_0}^{t_w} dt' D^* n_e S_h(t_w, t') & \text{for } t_w > t_0 \end{cases} + O(\varepsilon), \quad (118)$$

with  $S_h$  defined in (82). Finally, using the replacements

$$T_w(t_w, t_0) \rightarrow (t, t_0) \quad (119)$$

$$n_c(n, n_s, n_e) \rightarrow (n, n_s, n_e) \quad (120)$$

$$(121)$$

equations (116) and (118) are re-dimensionalized giving

$$n(t) = \frac{n_s + n_e e^{\Sigma(t-t_0)}}{1 + e^{\sigma(t-t_0)}}, \quad (122)$$

$$S(t) = \begin{cases} S_* S_h(t, t_*) + \int_{t_*}^t dt' D n_s S_h(t, t') & \text{for } t \leq t_0 \\ S_c S_h(t, t_0) + \int_{t_0}^t dt' D n_e S_h(t, t') & \text{for } t > t_0 \end{cases} \quad (123)$$

with the definitions

$$\Sigma = B A S_c \cos(\Omega t_0 + \phi) - B D (S_c - 1) n_s \quad (124)$$

$$\Omega = \frac{\omega}{T_w} \quad (125)$$

$$D = \frac{D^*}{T_w n_c} \quad (126)$$

$$A = \frac{g L_i \hat{w}}{c_p R_v T_{00}^2} \quad (127)$$

and the dimensional GW vertical velocity amplitude  $\hat{w}$ .

*g. Reduced ice physics model*

In order to evaluate the asymptotic parameterization derived in the previous section, we introduce a reference model. This model contains only the dominant terms from the full ice physics model in (46), (48) evaluated at level  $z_{00}$ , in dimensional form it reads

$$\frac{dn}{dt} = J \exp(B(S - S_c)), \quad (128)$$

$$\frac{dS}{dt} = -D(S - 1)n + SA \cos(\Omega t + \phi), \quad (129)$$

with  $A$  defined in (127).

## 4. Numerical experiments and discussion of the asymptotic solution

*a. Numerical verification of the asymptotic limit*

First, we demonstrate that the reference model (128),(129) converges for  $\varepsilon \rightarrow 0$  to the asymptotic solution (122), (123). In accordance with the scalings in (46), (48) we set

$$J = \varepsilon^{-1}, B = \varepsilon^{-2}, D = 1, \quad (130)$$

and integrate (128),(129) with initial conditions  $n(0) = 2 \times 10^6 \text{ kg}^{-1}$  and  $S(0) = 1$ . Fig. 1(a) shows that the asymptotic solution reproduces the model reasonably well already for  $\varepsilon = 0.2$ . The model converges quickly to the asymptotic solution, if we further decrease  $\varepsilon$  to 0.1: see Fig. 1(b).

*b. Comparison of the asymptotic model with simulations of reduced ice microphysics model*

Next, we compare the asymptotic parameterization and the reduced model for realistic parameter values taken from BS19 and summarized in tab. 2. The results are shown in Fig. 2 for two representative initial GW phases. The asymptotic solution reproduces with a high-accuracy the time evolution of the ice crystal number concentration and saturation ratio. The time of the nucleation event is captured as well. This is even the case for subsequent nucleation events: see Fig. 2(b). Since the phase of the GW is typically unknown in models, we study the sensitivity

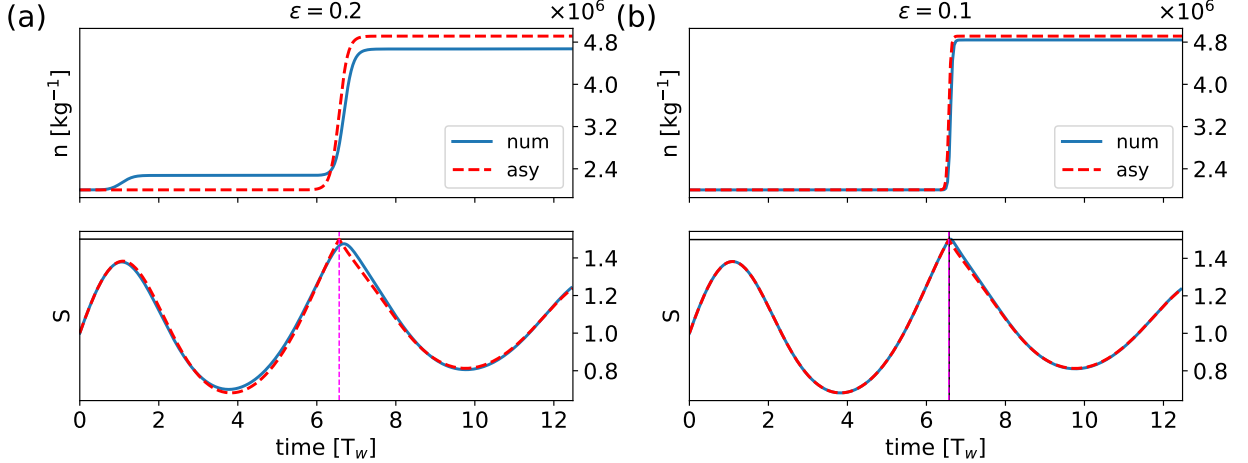


FIG. 1. Time evolution of number concentration  $n$  and saturation ratio  $S$  for  $\varepsilon = 0.2$  (a) and  $\varepsilon = 0.1$  (b) from the asymptotic solution (122),(123) and from the numerical integration of the reduced model (128),(129). In the plots for  $S$  the critical value  $S_c = 1.5$  is indicated by the solid horizontal line, the vertical dashed line denotes the time of the nucleation event  $t_0$  from the asymptotic condition (108) and the vertical solid line the corresponding time in the numerical simulation. Note, that for  $\varepsilon = 0.2$  the numerical solution does not reach  $S_c$ . The GW forcing amplitude is set in the calculations to  $A = 0.6T_w^{-1}$ , which corresponds to a GW amplitude of approximately  $0.7W_c$ , where  $W_c$  is the critical amplitude of the vertical velocity due to static instability breaking. The GW frequency is  $\Omega = T_w^{-1}$  with  $T_w = 500$  s and the initial GW phase is  $\phi = 0$ . The other initial conditions are  $S(0) = 1$  and  $n(0) = 2 \times 10^6 \text{ kg}^{-1}$ .

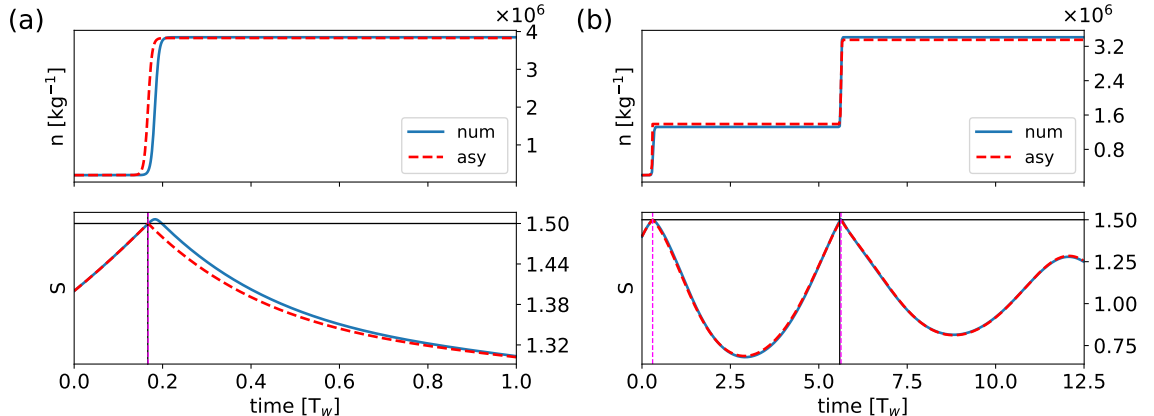


FIG. 2. Time evolution of number concentration  $n$  and saturation ratio  $S$  for an initial GW phase  $\phi = -\frac{\pi}{4}$  (a) and  $\phi = \frac{3\pi}{10}$  (b). The initial conditions are set to  $S(0) = 1.4$  and  $n(0) = 2 \times 10^5 \text{ kg}^{-1}$ . See the caption of Fig. 1 and Sec. 4b for further details.

of the results with respect to this parameter. For that purpose we vary the GW phase at the initial time  $t = 0$  and determine a final number concentration of nucleated ice crystals. This final number concentration is achieved after one or several subsequent nucleation events and is plotted in Fig. 3. From the Figure it is visible that the asymptotic solution captures the final number of nucleated ice crystals for all GW phases. In addition, the values of  $n$  are limited by the asymptotic

estimates represented by solid horizontal lines in the Figure: from above by  $N_{post}^{max}$  in (111) and from below by  $N_{pre}^{max}$  in (112). Further analysis showed that the region of the spike in  $n$ , for initial GW phase slightly below 1, is associated with multiple nucleation events. Outside this region only one nucleation event is observed in the asymptotic and in the numerical solutions. In this case the number of ice crystals after the first nucleation is sufficiently high, so that at all later times  $S$  remains below  $S_c$  due to the diffusional growth term. In Fig. 4 the difference between the

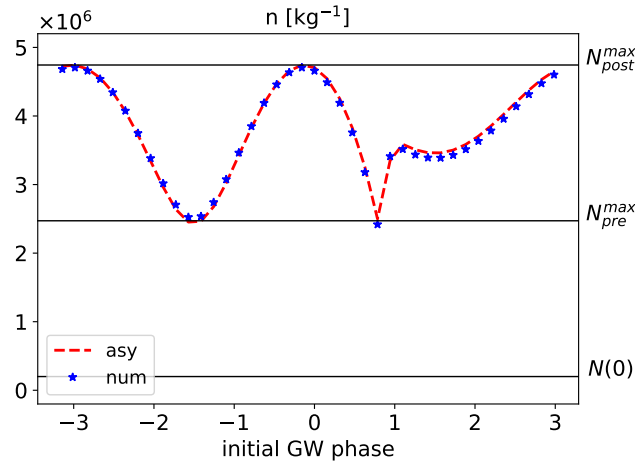


FIG. 3. Final number concentration  $n$  as a function of the initial GW phase for the asymptotic solution (122),(123) and for the numerical integration of the reduced model (128),(129). Solid horizontal lines denote the initial condition  $n(0)$  and the asymptotic estimates  $N_{pre}^{max}$  and  $N_{post}^{max}$  from equations (111) and (112), respectively. The initial conditions are set to  $S(0) = 1.4$  and  $n(0) = 2 \times 10^5 \text{ kg}^{-1}$ . See Sec. 4b and the caption of Fig. 1 for further details.

nucleation instant  $t_0$  within the first GW period and  $t_\phi$  is plotted, where  $t_\phi$  is the time of maximal GW forcing, i.e.,  $\cos(\Omega t_\phi + \phi) = 1$ . The Figure suggests that during nucleation the GW forcing is not far from its maximum. There is a jump in  $t_0 - t_\phi$  of about  $2\pi$  at GW phase equal to 1, as mentioned before multiple nucleation events are observed around this phase. The normalized vertical velocity at nucleation is displayed in Fig. 4 too and it shows that nucleation takes place only at sufficiently high updrafts.

Fig. 5 summarizes the dependence of the nucleated ice crystals on the initial number concentration. The asymptotic solution reproduces nearly exactly the number of newly generated ice crystals, as well as, it is able to capture the regimes without nucleation events.

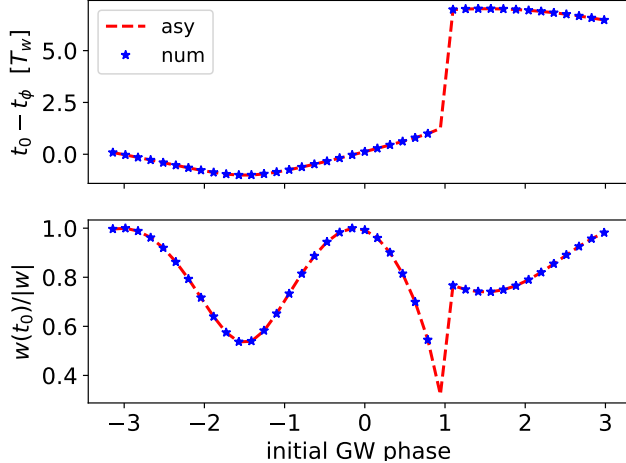


FIG. 4. The time difference  $t_0 - t_\phi$  and the normalized GW amplitude at  $t_0$  as a function of the initial GW phase for the models in Fig. 3. See Sec. 4b for further details. Note that for GW phase close to 1 S from the reference model does not reach  $S_c$  within the first GW period, because of this the corresponding data point "num" is missing in the plot.

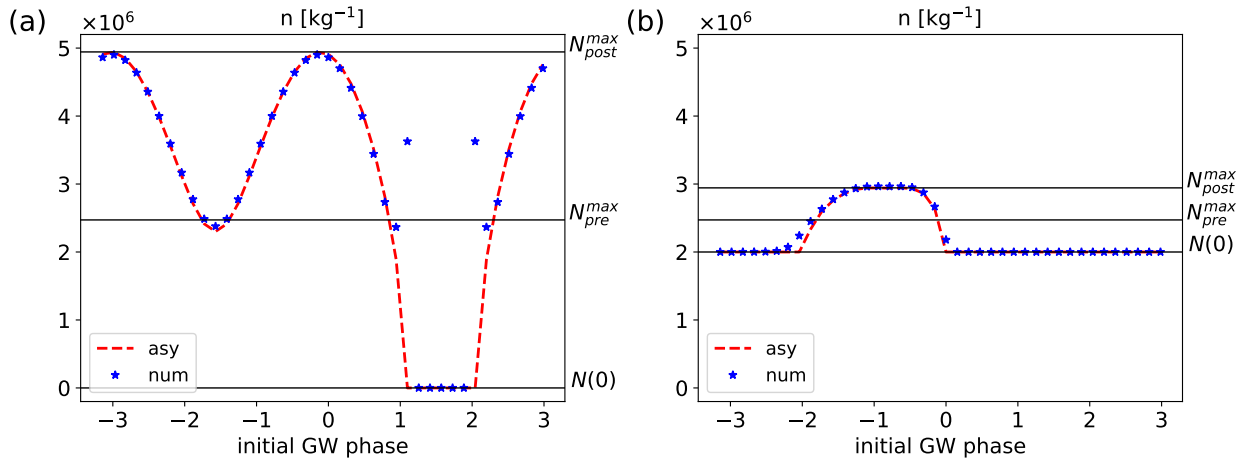


FIG. 5. As in Fig. 3 but for initial number concentration  $n(0) = 0$  (a) and  $n(0) = 2 \times 10^6 \text{ kg}^{-1}$  (b).

## 5. The effect of variable ice crystal mean mass

Performing realistic air parcel simulations with a box model and a bulk microphysics scheme, BS19 demonstrated that for a wide variety of environmental conditions the constant mean mass assumption is a reasonable approximation during nucleation. However, right before a nucleation event where the saturation ratio is above one, the mean mass of the ice crystals will grow leading to an increased deposition term, see the  $\bar{m}$  dependence in (29). The increased deposition will influence the saturation ratio, which on the other hand will affect the number of nucleated ice crystals. Since the mean mass of the ice crystals can be diagnosed from the relation  $m = q/n$

for  $n > 0$ , such effects can be incorporated in the present model if the evolution equation for  $q$  is included and the substitution  $\bar{m} = m(t) = q/n$  is introduced in the diffusional growth term. By considering again only the dominant term in the prognostic equations, this results in the following system of reduced equations

$$\frac{dn}{dt} = \frac{J^*}{\varepsilon} \exp\left(\frac{B^*}{\varepsilon^2}(S - S_c)\right) \quad (131)$$

$$\frac{dS}{dt} = -D^* \left(\frac{q}{n}\right)^{\frac{1}{3}} (S - 1)n + SA^* \cos(\omega t + \phi), \quad (132)$$

$$\frac{dq}{dt} = \frac{D^*}{\varepsilon} \left(\frac{q}{n}\right)^{\frac{1}{3}} (S - 1)n. \quad (133)$$

The corresponding dimensional form reads

$$\frac{dn}{dt} = J \exp(B(S - S_c)) \quad (134)$$

$$\frac{dS}{dt} = -D_0 \left(\frac{q}{n}\right)^{\frac{1}{3}} (S - 1)n + SA \cos(\Omega t + \phi), \quad (135)$$

$$\frac{dq}{dt} = D_q \left(\frac{q}{n}\right)^{\frac{1}{3}} (S - 1)n \quad (136)$$

where the depositional coefficients are defined as

$$D_0 = \frac{D}{m_c^{1/3}}, \quad D_q = \frac{D q_{v,c}}{m_c^{1/3}}, \quad (137)$$

with  $D$  and  $A$  given by (126) and (127), respectively.

In Fig. 6 we show simulations of the reference model with constant and with variable mean mass, in both cases the ice crystal mass is diagnosed using  $m = q/n$ . As expected, an increase of the ice crystal mass is observed before the nucleation event. Taking this into account with the model (131)-(133) results in larger number of nucleated ice particles, as compared to the constant mass model. In the following, we extend the asymptotic approach to allow for such variable mean mass effects.

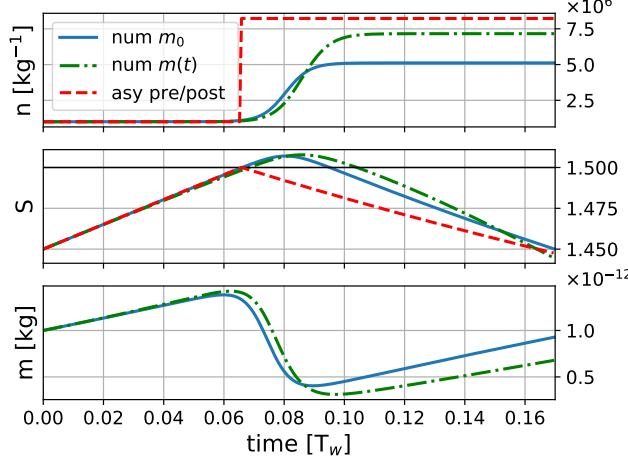


FIG. 6. Time evolution of number concentration  $n$ , saturation ratio  $S$  and mean ice mass  $m$  computed for three different models: the constant mean mass model (128),(129), the variable mean mass model (134)-(136) and the asymptotic solution from Sec. 5. The different models are denoted with  $m_0, m(t)$  and *asy*, respectively. The forcing amplitude is set to  $A = 0.75 T_w^{-1}$ , corresponding to a GW vertical velocity amplitude of approximately  $\hat{w} = 0.9 W_c$ . The  $m_0$  model integrates in addition to (128),(129) the equation for the ice mixing ratio (136) with a constant ratio  $q/n = 1$  on the right hand side. In the models  $m_0$  and  $m(t)$  the mean mass is diagnosed by using  $m = q/n$ . The initial conditions for all models are set to  $S(0) = 1.45$ ,  $n(0) = 10^6 \text{ kg}^{-1}$  and  $\phi = 0$ .

### a. Pre-nucleation regime

The fully coupled system (131)-(133) involves an additional fast time scale in the  $q$ -equation as compared to the constant mean mass case discussed in Sec. 3. The corresponding rigorous asymptotic analysis of the pre-nucleation regime is out of the scope of this paper, however, as we will show here, the asymptotic pre-nucleation solution for the constant mass case can still be used if appropriate corrections are introduced.

First, we observe in Fig. 6 that before nucleation the solution for  $S$  does not change much if the variable mean mass effect is taken into account. This motivates us to use the asymptotic solution (81) for  $S$  to compute the time,  $t_0$ , of the nucleation event from (108). For  $S - S_c = O(1) < 0$  the right-hand-side of (134) vanishes at leading order, implying the constant solution  $n(t) = N_{pre}$ . Using the latter result and integrating (136) from  $t_*$  up to  $t_0$ , we obtain at the end of the pre-nucleation regime

$$q(t_0)^{\frac{2}{3}} = D_q N_{pre}^{\frac{2}{3}} \int_{t_*}^{t_0} dt' (S(t') - 1) + q(t_*)^{\frac{2}{3}}, \quad (138)$$

with  $S(t)$  from (81).

*b. Nucleation regime*

Next, we consider the nucleation regime. On the fast nucleation time  $\tau$  we have the following system of equations

$$\frac{dn}{d\tau} = \varepsilon J^* \exp\left(\frac{B^*}{\varepsilon^2}(S - S_c)\right) \quad (139)$$

$$\frac{dS}{d\tau} = -\varepsilon^2 D^* \left(\frac{q}{n}\right)^{1/3} (S - 1)n + \varepsilon^2 S A^* \cos\left(\omega(t_0 + \varepsilon^2 \tau) + \phi\right), \quad (140)$$

$$\frac{dq}{d\tau} = \varepsilon D^* \left(\frac{q}{n}\right)^{1/3} (S - 1)n \quad (141)$$

From (141) we see that the leading order ice mixing ratio is constant during nucleation

$$q^{(0)}(\tau) = q_{pre}^{(0)}(t_0), \quad (142)$$

with the value of  $q_{pre}^{(0)}(t_0)$  from (138). Next, by repeating the manipulations in equations (90) to (94), one obtains from (139), (140) the following evolution equation for the number concentration

$$\frac{dn^{(0)}}{d\tau} + \tilde{\delta}(n^{(0)})^{5/3} - \gamma n^{(0)} = \tilde{\mu}, \quad (143)$$

with the constant

$$\tilde{\delta} = \frac{3}{5} \left(q^{(0)}\right)^{1/3} B^* D^* (S_c - 1) \quad (144)$$

$$(145)$$

and  $\gamma$  defined in (96). Eq (143) can be solved numerically to find the number concentration during the nucleation regime. The numerical integration of the ODE can be avoided if only the final  $n$  at the end of the nucleation is of interest. Proceeding as in Sec. 3e we have the following matching

conditions for the pre-nucleation, nucleation and post-nucleation regime

$$n_{nuc}^{(0)}(-\infty) = N_{pre}, \quad (146)$$

$$n_{nuc}^{(0)}(\infty) = N_{post}, \quad (147)$$

$$\frac{dn_{nuc}^{(0)}}{d\tau}(\pm\infty) = \frac{dn_{pre}^{(0)}}{dt}(t_0) = \frac{dn_{post}^{(0)}}{dt}(t_0) = 0 \quad (148)$$

Inserting the matching conditions in (143) leads to an algebraic equation for  $N_{post}$

$$\tilde{\delta}N_{post}^{5/3} - \gamma N_{post} = \tilde{\mu}, \quad (149)$$

where  $\tilde{\mu} = \tilde{\delta}N_{pre}^{5/3} - \gamma N_{pre}$ . Note that for  $N_{pre} = 0$ , (149) implies for the dependence of  $N_{post}$  on the GW vertical velocity:  $N_{post} \sim \hat{w}^{3/2}$ , which is consistent with the scaling in Kärcher and Lohmann (2002).

### c. Numerical results

Equation (149) is used to find an asymptotic approximation of the nucleated number concentration, the comparison with the numerical results is shown in Fig. 6. The current procedure allows to produce larger number of nucleated ice crystals as compared with the constant mass model, the magnitude of  $n$  is close to the one of the variable mean mass model.

The performance of the current approach is systematically evaluated by varying the initial GW phase. The corresponding results are summarized in Fig. 7. The figure suggests that the proposed procedure captures the number of ice crystals after nucleation for various initial GW phases, as well as, situations where the ice crystals evaporate (corresponding to points in the plot with  $n = 0$ ).

A note of caution should be added on the relevance of the variable mean mass model presented in this section. Fig. 6 suggests that there might be situations with considerable growth of  $m$  before nucleation takes place. Obviously, for large  $m$  the sedimentation term will provide a sink for the mean mass: see (47). The correct incorporation of the sedimentation effects will be subject of a future study.

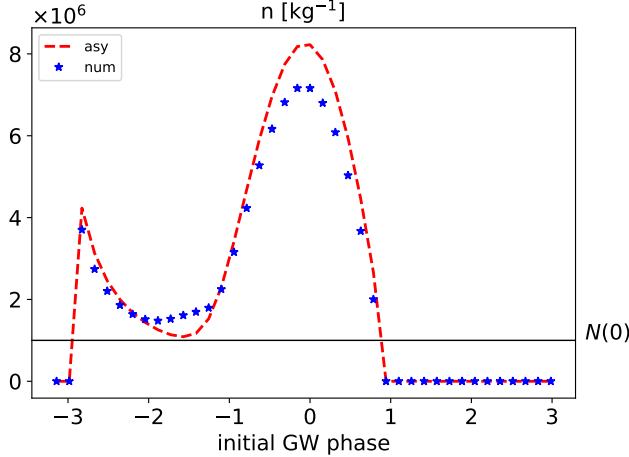


FIG. 7. Number concentration  $n$  as a function of the initial GW phase for the variable mean mass model (134)-(136) and for the asymptotic solution from Sec. 5. Initial conditions as in Fig. 6. Shown is the number concentration after the first nucleation event, but  $n$  is set to zero if the ice crystals evaporate before its occurrence.

## 6. Conclusions

We present an asymptotic approach allowing to identify a reduced model for the self-consistent description of ice physics forced by GW, including the effect of diffusional growth and homogeneous nucleation of ice crystals. Further, using matched asymptotic techniques analytical solutions are constructed, involving a novel parameterization for the ice crystal number concentration. The numerical simulations with the reduced ice physics model show that the parameterization reproduces nucleation events triggered by a monochromatic GW.

When comparing the treatment of the ice physics in our approach with the one from BS19, we observe different scaling in the nucleation term: in the latter work  $J \sim B \sim \varepsilon^{-1}$  is used, whereas here we apply  $J \sim \varepsilon^{-1}, B \sim \varepsilon^{-2}$ . Nevertheless, our parameterization (110) is equivalent to the closure of BS19 for constant updraft velocity if the velocity there is replaced by the GW vertical velocity at the nucleation time  $t_0$ . This is not surprising, since the GW nearly does not vary on the fast nucleation time scale. The correspondence of the two parameterizations becomes more clear if one takes into account that in BS19  $\varepsilon = O(10^{-2})$  and here  $\varepsilon = O(10^{-1})$ , implying the same magnitude of the nucleation exponent  $B$  under the different scalings. As shown by Spichtinger et al. (2022) the exact value of the nucleation rate  $J$  is not crucial as long as it is sufficiently large.

The parameterization (110) allowed us to derive upper and lower bounds for the number of nucleated ice crystals, as well as, a threshold for the initial number of ice crystal which will inhibit

nucleation. To our knowledge current cirrus parameterizations do not respect such bounds when GW fluctuations are taken into account.

The present parameterization is applicable to the mid-frequency GW in the upper troposphere and tropopause region, as well as, to high-frequency GW in the upper troposphere. For high-frequency GW in the tropopause region the ratio between the time scale of the diffusional growth and of the wave is given by  $T_d/T_w \sim \varepsilon^{-1}$ . In this case the asymptotic analysis suggests a new regime dominated by the GW forcing term. We expect that the latter regime corresponds to the temperature-limit events studied in Dinh et al. (2016). From (14) and (75) it follows that  $|\tilde{w}^{(0)}| = |\omega/m|$  implying diverging GW amplitudes for  $m \rightarrow 0$ . This limit is consistent with the high-frequency GW and forcing-dominated regime we mentioned above. For low-frequency GW the scaling  $T_d/T_w \sim \varepsilon$  is appropriate. In this case the GW forcing term becomes by a factor of  $\varepsilon$  weaker, when compared to the depositional growth term. This regime is relevant for low updraft velocities and will be considered in an upcoming study.

In the present regime the magnitude of the sedimentation effects is determined by the sedimentation time scale  $T_{sed} = H_c/c_q m_c^{2/3}$ . Substituting the reference quantities gives  $T_{sed} \sim \varepsilon^{-2} T_d \sim 11$  h, implying that at leading order sedimentation is negligible compared to the diffusional growth term. Note however, that  $T_{sed}$  will decrease if regimes with larger ice crystal mass,  $m_c$ , or smaller vertical scales,  $H_c$ , are of interest. As shown in Podglajen et al. (2018), sedimentation modulated by GW forcing produces localization effects in cirrus.

In the present study only cirrus formed by homogeneous nucleation are considered, since this is the dominant formation mechanism in the cold temperature regime with strong updraft velocities (e.g., Heymsfield and Miloshevich 1993). Still, heterogeneous nucleation can considerably alter the cirrus formation (see, e.g., Gierens 2003; Spichtinger and Cziczo 2010); however, the important feature is also in case of competing nucleation pathways the occurrence of pre-existing ice crystals, as in our investigations. In addition, turbulence due to GW breaking is an important source of GW generated variability omitted in the present study.

In future, we plan to extend the present analysis to the case with multiple GWs driving the ice physics. In addition, we will complement the theoretical investigations by numerical studies of cirrus in wave resolving simulations for more complete description of the GW-cirrus interactions.

*Acknowledgments.* UA and PS thank the German Research Foundation (DFG) for partial support through the research unit Multiscale Dynamics of Gravity Waves (MS-GWaves), TRR 301 – Project-ID 428312742 “TPChange” Projects B06 “Impact of small-scale dynamics on UTLS transport and mixing” and B07 “Impact of cirrus clouds on tropopause structure”, and through Grants AC 71/8-2, AC 71/8-2, and AC 71/12-2. UA acknowledges partial support through Grant CRC 181 “Energy transfers in Atmosphere and Ocean”, Project Number 274762653, Projects W01 “Gravity-wave parameterization for the atmosphere” and S02 “Improved Parameterizations and Numerics in Climate Models.”

*Data availability statement.* The Python script used to generate all figures in the paper is available upon request.

## References

Achatz, U., 2022: *Atmospheric Dynamics*. Springer Berlin Heidelberg, Berlin, Heidelberg, <https://doi.org/10.1007/978-3-662-63941-2>, URL <https://link.springer.com/10.1007/978-3-662-63941-2>.

Achatz, U., R. Klein, and F. Senf, 2010: Gravity waves, scale asymptotics and the pseudo-incompressible equations. *Journal of Fluid Mechanics*, **663**, 120–147, <https://doi.org/10.1017/S0022112010003411>, URL [https://www.cambridge.org/core/product/identifier/S0022112010003411/type/journal\\_article](https://www.cambridge.org/core/product/identifier/S0022112010003411/type/journal_article).

Achatz, U., B. Ribstein, F. Senf, and R. Klein, 2017: The interaction between synoptic-scale balanced flow and a finite-amplitude mesoscale wave field throughout all atmospheric layers: weak and moderately strong stratification. *Quarterly Journal of the Royal Meteorological Society*, **143 (702)**, 342–361, <https://doi.org/10.1002/qj.2926>, URL <https://onlinelibrary.wiley.com/doi/10.1002/qj.2926>.

Baumgartner, M., C. Rolf, J.-U. Grooß, J. Schneider, T. Schorr, O. Möhler, P. Spichtinger, and M. Krämer, 2022: New investigations on homogeneous ice nucleation: the effects of water activity and water saturation formulations. *Atmospheric Chemistry and Physics*, **22 (1)**, 65–91, <https://doi.org/10.5194/acp-22-65-2022>, URL <https://acp.copernicus.org/articles/22/65/2022/>, publisher: Copernicus GmbH.

Baumgartner, M., and P. Spichtinger, 2019: Homogeneous nucleation from an asymptotic point of view. *Theoretical and Computational Fluid Dynamics*, **33** (1), 83–106, <https://doi.org/10.1007/s00162-019-00484-0>, URL <http://link.springer.com/10.1007/s00162-019-00484-0>.

Baumgartner, M., R. Weigel, A. H. Harvey, F. Plöger, U. Achatz, and P. Spichtinger, 2020: Reappraising the appropriate calculation of a common meteorological quantity: potential temperature. *Atmospheric Chemistry and Physics*, **20** (24), 15 585–15 616, <https://doi.org/10.5194/acp-20-15585-2020>, URL <https://acp.copernicus.org/articles/20/15585/2020/>, publisher: Copernicus GmbH.

Bramberger, M., and Coauthors, 2022: First Super-Pressure Balloon-Borne Fine-Vertical-Scale Profiles in the Upper TTL: Impacts of Atmospheric Waves on Cirrus Clouds and the QBO. *Geophysical Research Letters*, **49** (5), e2021GL097596, <https://doi.org/10.1029/2021GL097596>, URL <https://onlinelibrary.wiley.com/doi/abs/10.1029/2021GL097596>, \_eprint: <https://onlinelibrary.wiley.com/doi/pdf/10.1029/2021GL097596>.

Bölöni, G., Y.-H. Kim, S. Borchert, and U. Achatz, 2021: Toward Transient Subgrid-Scale Gravity Wave Representation in Atmospheric Models. Part I: Propagation Model Including Nondissipative Wave–Mean-Flow Interactions. *Journal of the Atmospheric Sciences*, **78** (4), 1317–1338, <https://doi.org/10.1175/JAS-D-20-0065.1>, URL <https://journals.ametsoc.org/view/journals/atsc/78/4/JAS-D-20-0065.1.xml>, publisher: American Meteorological Society Section: Journal of the Atmospheric Sciences.

Bölöni, G., B. Ribstein, J. Muraschko, C. Sgoff, J. Wei, and U. Achatz, 2016: The Interaction between Atmospheric Gravity Waves and Large-Scale Flows: An Efficient Description beyond the Nonacceleration Paradigm. *Journal of the Atmospheric Sciences*, **73** (12), 4833–4852, <https://doi.org/10.1175/JAS-D-16-0069.1>, URL <https://journals.ametsoc.org/view/journals/atsc/73/12/jas-d-16-0069.1.xml>, publisher: American Meteorological Society Section: Journal of the Atmospheric Sciences.

Dean, S. M., J. Flowerdew, B. N. Lawrence, and S. D. Eckermann, 2007: Parameterisation of orographic cloud dynamics in a GCM. *Climate Dynamics*, **28** (6), 581–597, <https://doi.org/10.1007/s00382-006-0202-0>, URL <http://link.springer.com/10.1007/s00382-006-0202-0>.

Dinh, T., A. Podglajen, A. Hertzog, B. Legras, and R. Plougonven, 2016: Effect of gravity wave temperature fluctuations on homogeneous ice nucleation in the tropical tropopause layer. *Atmospheric Chemistry and Physics*, **16** (1), 35–46, <https://doi.org/10.5194/acp-16-35-2016>, URL <https://acp.copernicus.org/articles/16/35/2016/>, publisher: Copernicus GmbH.

Durran, D. R., 1989: Improving the Anelastic Approximation. *Journal of the Atmospheric Sciences*, **46** (11), 1453–1461, [https://doi.org/10.1175/1520-0469\(1989\)046<1453:ITAA>2.0.CO;2](https://doi.org/10.1175/1520-0469(1989)046<1453:ITAA>2.0.CO;2), URL [https://journals.ametsoc.org/view/journals/atsc/46/11/1520-0469\\_1989\\_046\\_1453\\_itaa\\_2\\_0\\_co\\_2.xml](https://journals.ametsoc.org/view/journals/atsc/46/11/1520-0469_1989_046_1453_itaa_2_0_co_2.xml), publisher: American Meteorological Society Section: Journal of the Atmospheric Sciences.

Gierens, K., 2003: On the transition between heterogeneous and homogeneous freezing. *Atmospheric Chemistry and Physics*, **3** (2), 437–446, <https://doi.org/10.5194/acp-3-437-2003>, URL <https://acp.copernicus.org/articles/3/437/2003/>.

Haag, W., and B. Kärcher, 2004: The impact of aerosols and gravity waves on cirrus clouds at midlatitudes. *Journal of Geophysical Research*, **109**, D12 202, <https://doi.org/10.1029/2004JD00457>.

Heymsfield, A. J., and L. M. Miloshevich, 1993: Homogeneous Ice Nucleation and Supercooled Liquid Water in Orographic Wave Clouds. *Journal of the Atmospheric Sciences*, **50** (15), 2335–2353, [https://doi.org/10.1175/1520-0469\(1993\)050<2335:HINASL>2.0.CO;2](https://doi.org/10.1175/1520-0469(1993)050<2335:HINASL>2.0.CO;2), URL [https://journals.ametsoc.org/view/journals/atsc/50/15/1520-0469\\_1993\\_050\\_2335\\_hinasl\\_2\\_0\\_co\\_2.xml](https://journals.ametsoc.org/view/journals/atsc/50/15/1520-0469_1993_050_2335_hinasl_2_0_co_2.xml), publisher: American Meteorological Society Section: Journal of the Atmospheric Sciences.

Holmes, M. H., 2013: *Introduction to Perturbation Methods*. Texts in Applied Mathematics, 20, Springer.

Hoose, C., and O. Möhler, 2012: Heterogeneous ice nucleation on atmospheric aerosols: a review of results from laboratory experiments. *Atmospheric Chemistry and Physics*, **12**, 9817–9854.

Jensen, E., and L. Pfister, 2004: Transport and freeze-drying in the tropical tropopause layer. *Journal of Geophysical Research*, **109** (D02207), <https://doi.org/10.1029/2003JD004022>.

Joos, H., P. Spichtinger, and U. Lohmann, 2009: Orographic cirrus in a future climate. *Atmospheric Chemistry and Physics*, **9** (20), 7825–7845, <https://doi.org/10.5194/acp-9-7825-2009>, URL <https://acp.copernicus.org/articles/9/7825/2009/>.

Joos, H., P. Spichtinger, U. Lohmann, J.-F. Gayet, and A. Minikin, 2008: Orographic cirrus in the global climate model ECHAM5. *Journal of Geophysical Research*, **113** (D18), D18 205, <https://doi.org/10.1029/2007JD009605>, URL <http://doi.wiley.com/10.1029/2007JD009605>.

Kienast-Sjögren, E., P. Spichtinger, and K. Gierens, 2013: Formulation and test of an ice aggregation scheme for two-moment bulk microphysics schemes. *Atmospheric Chemistry and Physics*, **13** (17), 9021–9037, <https://doi.org/10.5194/acp-13-9021-2013>, URL <https://acp.copernicus.org/articles/13/9021/2013/>.

Kim, J.-E., and Coauthors, 2016: Ubiquitous Influence of Waves on Tropical High Cirrus Cloud. *Geophysical Research Letters*, **43**, 5895–5901, <https://doi.org/10.1002/2016GL069293>.

Kim, Y.-H., G. Bölöni, S. Borchert, H.-Y. Chun, and U. Achatz, 2021: Toward Transient Subgrid-Scale Gravity Wave Representation in Atmospheric Models. Part II: Wave Intermittency Simulated with Convective Sources. *Journal of the Atmospheric Sciences*, **78** (4), 1339–1357, <https://doi.org/10.1175/JAS-D-20-0066.1>, URL <https://journals.ametsoc.org/view/journals/atsc/78/4/JAS-D-20-0066.1.xml>, publisher: American Meteorological Society Section: Journal of the Atmospheric Sciences.

Koop, T., B. Luo, A. Tsias, and T. Peter, 2000: Water activity as the determinant for homogeneous ice nucleation in aqueous solutions. *Nature*, **406** (6796), 611–614, <https://doi.org/10.1038/35020537>, URL <http://www.nature.com/articles/35020537>.

Krämer, M., and Coauthors, 2016: A microphysics guide to cirrus clouds – Part 1: Cirrus types. *Atmospheric Chemistry and Physics*, **16** (5), 3463–3483, <https://doi.org/10.5194/acp-16-3463-2016>, URL <https://acp.copernicus.org/articles/16/3463/2016/>.

Krämer, M., and Coauthors, 2020: A microphysics guide to cirrus – Part 2: Climatologies of clouds and humidity from observations. *Atmospheric Chemistry and Physics*, **20** (21), 12 569–12 608, <https://doi.org/10.5194/acp-20-12569-2020>, URL <https://acp.copernicus.org/articles/20/12569/2020/>, publisher: Copernicus GmbH.

Kärcher, B., and U. Lohmann, 2002: A parameterization of cirrus cloud formation: Homogeneous freezing of supercooled aerosols. *Journal of Geophysical Research: Atmospheres*, **107** (D2), AAC 4–1–AAC 4–10, <https://doi.org/10.1029/2001JD000470>, URL <https://onlinelibrary.wiley.com/doi/abs/10.1029/2001JD000470>, \_eprint: <https://onlinelibrary.wiley.com/doi/pdf/10.1029/2001JD000470>.

Kärcher, B., and A. Podglajen, 2019: A Stochastic Representation of Temperature Fluctuations Induced by Mesoscale Gravity Waves. *Journal of Geophysical Research: Atmospheres*, **124** (21), 11 506–11 529, <https://doi.org/10.1029/2019JD030680>, URL <https://onlinelibrary.wiley.com/doi/abs/10.1029/2019JD030680>, \_eprint: <https://onlinelibrary.wiley.com/doi/pdf/10.1029/2019JD030680>.

Kärcher, B., and J. Ström, 2003: The roles of dynamical variability and aerosols in cirrus cloud formation. *Atmospheric Chemistry and Physics*, **3** (3), 823–838, <https://doi.org/10.5194/acp-3-823-2003>, URL <https://acp.copernicus.org/articles/3/823/2003/>, publisher: Copernicus GmbH.

Lohmann, U., and B. Kärcher, 2002: First interactive simulations of cirrus clouds formed by homogeneous freezing in the ECHAM general circulation model. *Journal of Geophysical Research: Atmospheres*, **107** (D10), AAC 8–1–AAC 8–13, <https://doi.org/10.1029/2001JD000767>, URL <https://onlinelibrary.wiley.com/doi/abs/10.1029/2001JD000767>, \_eprint: <https://onlinelibrary.wiley.com/doi/pdf/10.1029/2001JD000767>.

Podglajen, A., A. Hertzog, R. Plougonven, and B. Legras, 2016: Lagrangian temperature and vertical velocity fluctuations due to gravity waves in the lower stratosphere. *Geophysical Research Letters*, **43** (7), 3543–3553, <https://doi.org/10.1002/2016GL068148>, URL <https://onlinelibrary.wiley.com/doi/abs/10.1002/2016GL068148>, \_eprint: <https://onlinelibrary.wiley.com/doi/pdf/10.1002/2016GL068148>.

Podglajen, A., R. Plougonven, A. Hertzog, and E. Jensen, 2018: Impact of gravity waves on the motion and distribution of atmospheric ice particles. *Atmospheric Chemistry and Physics*, **18** (14), 10 799–10 823, <https://doi.org/10.5194/acp-18-10799-2018>, URL <https://acp.copernicus.org/articles/18/10799/2018/>, publisher: Copernicus GmbH.

Pruppacher, H., and J. Klett, 2010: *Microphysics of Clouds and Precipitation*. Springer, URL <https://link.springer.com/book/10.1007/978-0-306-48100-0>.

Spichtinger, P., and D. Cziczo, 2010: Impact of heterogeneous ice nuclei on homogeneous freezing events. *Journal of Geophysical Research*, **115**, <https://doi.org/10.1029/2009JD012168>.

Spichtinger, P., and K. M. Gierens, 2009: Modelling of cirrus clouds – Part 1a: Model description and validation. *Atmospheric Chemistry and Physics*, **9** (2), 685–706, <https://doi.org/10.5194/acp-9-685-2009>, URL <https://acp.copernicus.org/articles/9/685/2009/>, publisher: Copernicus GmbH.

Spichtinger, P., and M. Krämer, 2013: Tropical tropopause ice clouds: a dynamic approach to the mystery of low crystal numbers. *Atmospheric Chemistry and Physics*, **13** (19), 9801–9818, <https://doi.org/10.5194/acp-13-9801-2013>, URL <https://www.atmos-chem-phys.net/13/9801/2013/>.

Spichtinger, P., P. Marschalik, and M. Baumgartner, 2022: Impact of formulations of the nucleation rate on ice nucleation events. *Atmospheric Chemistry and Physics Discussions*, 1–43, <https://doi.org/10.5194/acp-2022-434>, URL <https://acp.copernicus.org/preprints/acp-2022-434/>, publisher: Copernicus GmbH.

Spreitzer, E. J., M. P. Marschalik, and P. Spichtinger, 2017: Subvisible cirrus clouds – a dynamical system approach. *Nonlinear Processes in Geophysics*, **24** (3), 307–328, <https://doi.org/10.5194/npg-24-307-2017>, URL <https://npg.copernicus.org/articles/24/307/2017/npg-24-307-2017-discussion.html>, publisher: Copernicus GmbH.

Wang, M., and J. E. Penner, 2010: Cirrus clouds in a global climate model with a statistical cirrus cloud scheme. *Atmospheric Chemistry and Physics*, **10** (12), 5449–5474, <https://doi.org/10.5194/acp-10-5449-2010>, URL <https://acp.copernicus.org/articles/10/5449/2010/>, publisher: Copernicus GmbH.

Zhang, Y., A. Macke, and F. Albers, 1999: Effect of crystal size spectrum and crystal shape on stratiform cirrus radiative forcing. *Atmospheric Research*, **52** (1-2), 59–75, [https://doi.org/10.1016/S0169-8095\(99\)00026-5](https://doi.org/10.1016/S0169-8095(99)00026-5).